ADVANCED FUNCTIONAL MATERIALS
www.afm-journal.de

Materials Views
www.MaterialsViews.com

Formation and Movement of Cationic Defects During Forming and Resistive Switching in $SrTiO_3$ Thin Film Devices

*Christian Lenser, Annemarie Koehl, Ivetta Slipukhina, Hongchu Du, Marten Patt, Vitaliy Feyer, Claus M. Schneider, Marjana Lezaic, Rainer Waser, and Regina Dittmann**

The resistance switching phenomenon in many transition metal oxides is described by ion motion leading to the formation of oxygen-deficient, highly electron-doped filaments. In this paper, the interface and subinterface region of electroformed and switched metal–insulator–metal structures fabricated from a thin Fe-doped $SrTiO_3$ (STO) film on n-conducting Nb-doped $SrTiO_3$ crystals are investigated by photoemission electron microscopy, transmission electron microscopy, and hard X-ray photoelectron spectroscopy in order to gain a deeper understanding of cation movement in this specific system. During electroforming, the segregation of Sr to the top interface and the generation of defect-rich cones in the film are observed, apparently growing from the anode toward the cathode during electroforming. An unusual binding energy component of the Sr 3d emission line is observed which can be assigned to $Sr''_{Ti}-V_O^{**}$ defect complexes by performing ab initio calculations. Since this Sr component can be reversibly affected by an external electrical bias, the movement of both oxygen and Sr point defects and the formation of defect complexes $Sr''_{Ti}-V_O^{**}$ during resistive switching are suggested. These findings are discussed with regard to the point defect structure of the film and the local oxidation of the donor-doped substrate. In particular, the apparent dichotomy between the observation of acceptor-type defects and increased electronic conductivity in STO is addressed.

1. Introduction

The reversible resistance change in transition metal oxide and other material systems under an applied electric field has drawn much research interest in the past 14 years, from both a scientific and a commercial viewpoint.[1–3] For transition metal oxides, $SrTiO_3$ is often regarded as a model system due the well-studied, systematic variations of its physical properties in dependence of oxidation state and doping.[4]

Most models proposed for the valence change mechanism (VCM) of the resistive switching process in oxides such as $SrTiO_3$ (STO) are based only on the electric field-induced movement of anionic defects, namely, oxygen vacancies V_O^{**} and the modification of the local dopant distribution that affects the Schottky-barrier at the active device interface.[4,5–7] The common assumption is that anionic defects in $SrTiO_3$ determine the nonvolatile resistance change due to the low activation energies of diffusion,[8–11] while cationic defects are much less mobile due to the high activation energy of diffusion.[12] Similarly, low cation diffusion coefficients are known since long for $BaTiO_3$,[13] which shows a very similar point defect chemistry as $SrTiO_3$.[14] In addition to the ionic mobilities, an indication of the oxygen vacancy-related phenomenon in STO single crystals and thin films has been provided by a variety of spectroscopic investigations.[15,16]

However, the filamentary resistive switching is often accompanied by very high local temperatures.[17] In particular, during the initial electroforming step, the temperatures may come close to the melting temperature of the oxide.[18] Under these severe conditions it is expected that also cationic defects are generated and moved in $SrTiO_3$ despite of their high formation and migration energies.

In fact, evidence for the movement of Sr ions under applied bias in resistive switching devices was recently established independently by our group and Kim and co-workers.[18–20] In general, the segregation of A-site cations during deposition, temperature treatment or oxidation/reduction of complex transition metal oxides is well known.[21–25] Regarding the impact of cationic defects and their movement during the electroforming and resistive switching of $SrTiO_3$, it is not yet known how such defects are generated, whether their movement or generation is reversible, and whether they are incorporated into the lattice or precipitated as secondary phases. In order to shed light on these issues, it is necessary to obtain more information about the local chemical state of the material at the interface in correlation to the resistance state.

Dr. C. Lenser, Dr. A. Koehl, Dr. I. Slipukhina, Dr. H. Du, M. Patt, Dr. V. Feyer, Prof. C. M. Schneider, Prof. M. Lezaic, Prof. R. Waser, Prof. R. Dittmann
Peter Grünberg Institut
Forschungszentrum Jülich
52425 Jülich, Germany
E-mail: r.dittmann@fz-juelich.de

DOI: 10.1002/adfm.201500851

In this paper, we employ a combination of microscopy and spectroscopy to study the chemical structure of Fe-doped $SrTiO_3$ (FeSTO) thin films epitaxially grown on n-conducting 0.5 wt% Nb-doped $SrTiO_3$ (NbSTO) single crystals. The study is conducted after electroforming and resistive switching of the FeSTO thin films. Photoemission electron microscopy (PEEM) and hard X-ray photoelectron spectroscopy (HAXPES) present strong evidence for significant, reversible Sr-diffusion under electrical bias, which we interpret as a product of the large temperature and potential gradients during electrical treatment. The observation of a Sr 3d emission line at uncommon binding energy is related to the creation of Sr antisite defects, according to density functional theory (DFT) calculations. By cross-sectional transmission electron microscopy (TEM) analysis we could show that the generation of the antisite defect on the surface goes along with the formation of filaments consisting of cationic vacancies growing from the anode during forming.

2. Local Cation Segregation During Electroforming

In order to investigate the chemical modifications induced by the forming and switching processes, we prepared three Au/FeSTO/NbSTO MIM (metal–insulator–metal)-structures in the virgin, ON and OFF state. The resistive switching characteristics of such devices is displayed in **Figure 1**a. During an initial soft-forming sweep to +5 V with a current compliance of 10 mA, the virgin resistance (>1 GΩ) is degraded into the kΩ regime (red line). To achieve the high-resistance OFF state, a negative bias is applied after forming, and a subsequent positive bias sets the device into the low-resistance ON state. Bipolar resistive switching is observed with an eightwise switching polarity, with $R_{OFF}/R_{ON} > 10^2$.[26] After electrical characterization, the top electrode is removed in order to allow the investigation of the former electrode interface with surface sensitive spectroscopy in the soft X-ray regime.

For the spectromicroscopic analysis with the PEEM, we utilized the highest absorption cross section for each element and combined X-ray absorption spectroscopy (XAS) at the Ti L-edge and the O K-edge with X-ray photoelectron spectroscopy (XPS) at the Sr 3d core level. From the stack of microscopy images recorded for variable photon energy (XAS) or binding energy (XPS), the corresponding spectra can be extracted by integrating the pixel intensity within defined regions of interest.

In Figure 1b, the microscopic contrast at the t_{2g}-level of the Ti L_3-absorption edge is presented for the three electrode pads in the virgin, OFF, and ON states. Images from $h\nu$ = 457.2 to 457.8 eV were averaged for better image quality. The electrode area is visible for all pads due to modifications of the surrounding $SrTiO_3$ surface by etching during lithography. The virgin pad reveals a uniform intensity across the whole pad area. In contrast, both pads which have been electrically treated show a large number of small spots with a diameter of up to 200 nm distributed over the entire pad area. The smallest detectable features had a size below 100 nm, which is limited by the resolution of the PEEM instrument. As

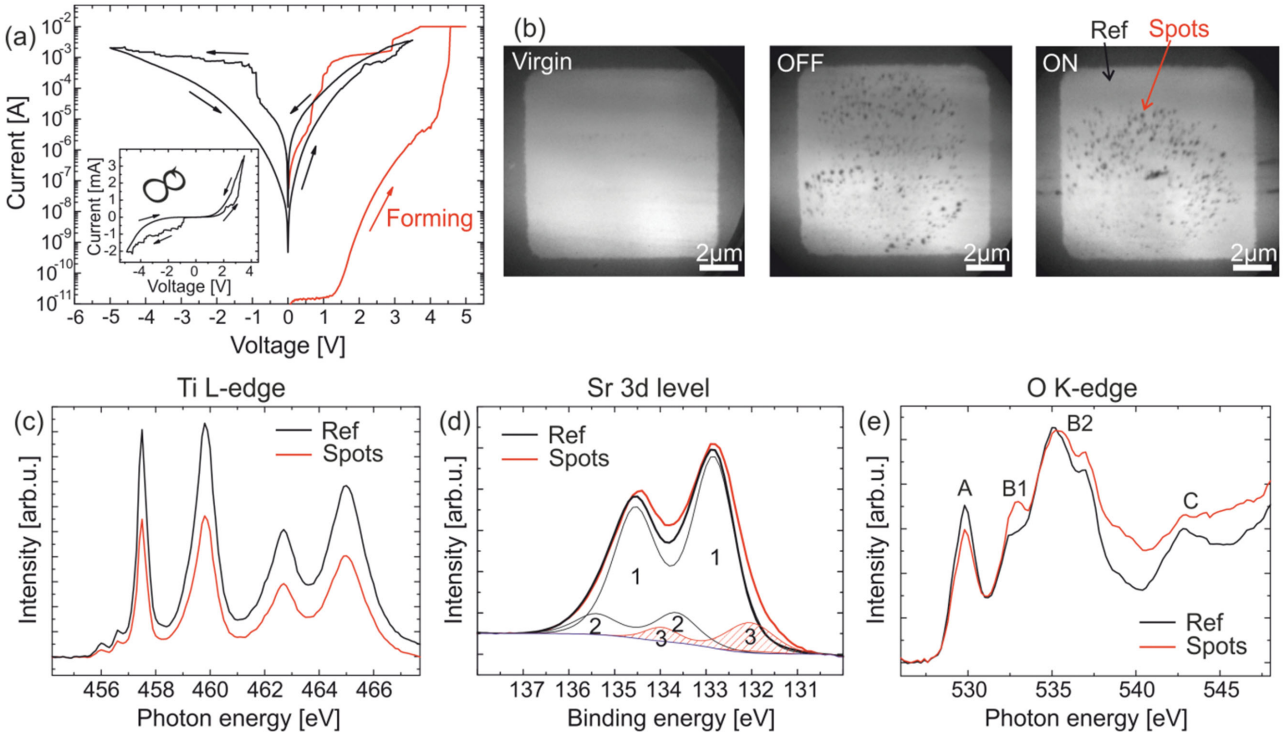

Figure 1. a) Eightwise resistive switching characteristics in $SrTiO_3$ thin film device. The red curve indicates the initial soft-forming sweep. The voltage refers to the top Au electrode. b) Microscopy images at the Ti absorption edge (averaged from $h\nu$ = 457.2– 457.8 eV) for pads in different resistive states. On the switched pads a spotlike pattern is observed which is expected to have developed during the forming procedure. c–e) Ti L-edge absorption, Sr 3d photoelectron and O K-edge absorption spectra for the region of the spots and an unchanged reference region. The Au top electrode was removed before the spectromicroscopic analysis.

this spot-like pattern is comparable for the ON and the OFF state, we assume that it develops during the initial forming step, which is an irreversible modification of the device and connected to higher currents (and correspondingly the presumably very high local temperatures) and voltages than the switching cycles.[18,27]

Figure 1c shows the Ti $L_{2,3}$-edge spectrum for a reference region from an apparently unchanged pad area next to the spots (black arrow). The spectrum is identical to a spectrum gained from the virgin pad and reveals the characteristic spin-orbit and crystal-field split structure of Ti^{4+} ions in octahedral coordination expected for $SrTiO_3$.[28] As already apparent from the microscopy image, the Ti intensity within the spots is considerably decreased. However, careful examination of the spectra reveals that no variation of the spectral line shape is present.

In contrast, an increased intensity at the low binding energy side is clearly observed for the Sr 3d XPS emission line measured at the same location, as displayed in Figure 1d. Using a peak-fitting model based on reference data collected on NbSTO single crystal and as-deposited FeSTO reference samples to establish the main peak parameters, we find that an accurate fit to the spectrum consists of three doublet components. The main component 1 is due to the contribution from the $SrTiO_3$ lattice and component 2 is due to surface SrO compounds.[22] Additionally, a low binding energy component ("3") is found roughly 0.8 eV below the STO main component in the spectra extracted from the location of the spots. As the relative intensity of component 3 in the spectra extracted from the PEEM images is massively influenced by the choice of the region of interest, it is not possible to reliably identify intensity differences between ON and OFF state. The occurrence of a low binding energy component in the Sr 3d spectrum has been observed previously,[19,29] but the origin of this spectral component is not yet understood.

We complement the spectroscopic analysis by inspecting the O K-edge spectrum displayed in Figure 1e. The reference region reveals the expected line shape with four main peaks (labeled A, B1, B2, and C) reported in literature for $SrTiO_3$.[30] The spectrum acquired within the region of the spots reveals distinct variations of the line shape—most notably a decrease of peak A and an increase of peak B1 compared to the reference and additional intensity in the minimum before peak C, which results in a significantly less pronounced peak C for the spots.

The reduced intensity of the Ti $L_{2,3}$-edge at the locations where the new Sr 3d component arises, as shown in Figure 1c, indicates an enrichment of Sr-related phases or defects on the surface. In the high-resolution SEM image of an ON pad shown in **Figure 2**b, the spotlike pattern observed in the PEEM (Figure 2a) can be clearly identified as surface segregations in the form of small islands.

The PEEM and SEM measurements confirm that a significant Sr diffusion toward the top interface is induced by the electrical treatment. Experimentally, this is observed by the occurrence of a low binding energy component in the Sr 3d emission line, the attenuation of the Ti signal and the formation of segregated islands.

Since both PEEM and SEM are surface sensitive techniques, a closer examination of the dimensionality of the observed segregations was performed with high-resolution transmission electron microscopy (HR-TEM) on a thin lamella fabricated using a focused ion beam (FIB) technique.

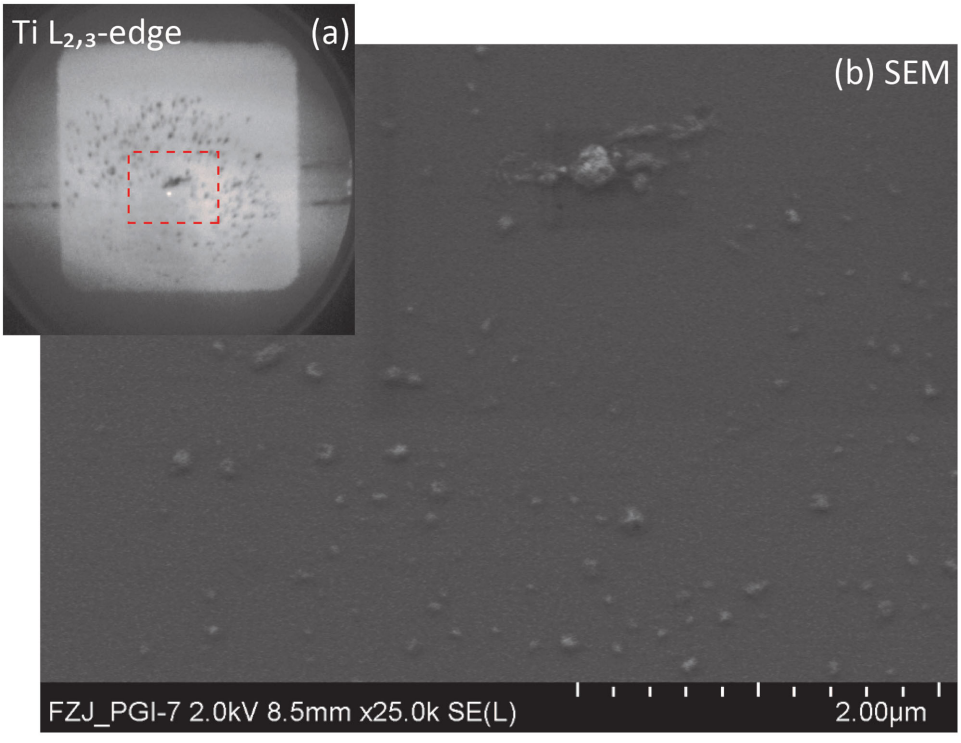

Figure 2. a) PEEM image indicating the location of the b) SEM image. The SEM image clearly shows the dark spots to be segregated islands on the surface. The higher spatial resolution (2–3 nm) of the SEM reveals segregations with a size down to approximately 10–20 nm.

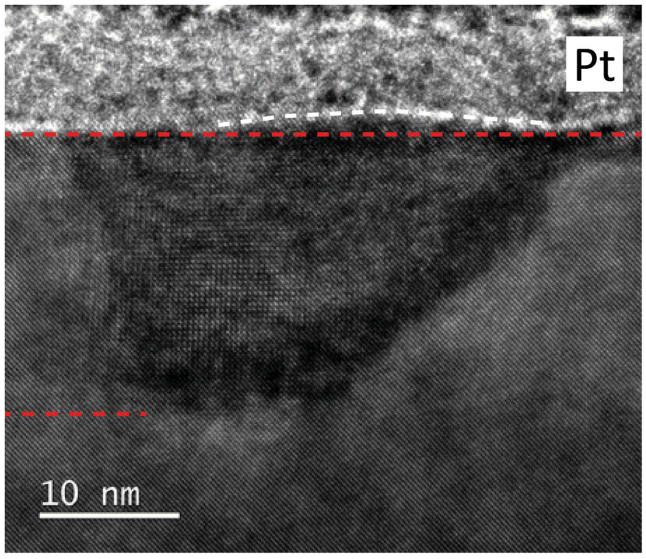

Figure 3. Bright field HR-TEM cross-section of a segregation spot. The red dashed lines indicate the top- and bottom-interfaces of the thin film, the white dashed line the curvature of the Pt deposited over a surface segregation.

The cross-sectional image recorded in the vicinity of such a segregation shown in **Figure 3**a clearly reveals that the observed changes are not limited to the surface. Underneath the surface segregation, which is visible as a small deformation of the Pt cover layer deposited during FIB preparation (indicated with a dashed white line), an extended zone of darker contrast in the shape of a truncated cone can be seen. The darker contrast of the cone compared to the matrix in the bright field image is due to a difference in orientation. This misorientation between the cone region and the matrix is likely due to lattice distortions caused by an increased amount of cation vacancy defects within the truncated cone region.[31] Reference lamellae cut from virgin electrodes did not show such features. Interestingly, the truncated cone extends across the entire thickness of the FeSTO film and is inverted, with the base at the top interface and the smaller apex at the bottom interface. It is interesting to note that the contrast modification seem to even extend into the NbSTO substrate underneath the cone region.

3. Ab Initio Calculations of the Defect Structure

In order to understand the defect configuration associated with the lower binding energy component at the Sr 3d emission line, it is necessary to correlate the spectral signature of this component to a chemical structure. An extensive literature research revealed no experimental reports of a Sr phase with a binding energy more than 0.5 eV below the $SrTiO_3$ binding energy. Therefore, we performed density functional theory calculations of electronic properties of potential defects in the $SrTiO_3$ crystal, which could be responsible for the observed results of the spectroscopic measurements.

In the literature, a complex antisite defect Sr''_{Ti}, which consists of a Sr ion on a Ti lattice site, has been reported for Sr-rich $SrTiO_3$ phases.[23,24] Therefore, we have considered such a defect by substituting one Ti atom by Sr in a 135 atomic supercell and removing one O atom in order to keep the simulation cell charge neutral. It should be noted that the oxygen vacancy (V_O^{**}) in a close vicinity of Sr''_{Ti} defect is essentially more stable than the one further away from the defect. Hence, only the results for the former case are presented in this work. In **Figure 4**a the corresponding defect structure after the relaxation is displayed, together with the Sr 3d core level position (b) and the calculated O K-edge spectrum (c). As follows from Figure 4b, compared to the undisturbed Sr ions further away from the defect, the 3d core level for the Sr at Ti site is shifted by approximately 0.8–0.9 eV to lower binding energies. Considering the experimental uncertainties and not taking into account the final state effects in our theoretical calculations, this value is in very good accordance to the experimentally observed one.

The changes of the intensity of the main peaks in the O K-edge spectrum (Figure 4c), calculated in Z + 1 approximation (to account for the core-hole effects),[32,33] are similar to those observed in our XAS spectra, if only the contribution from the O atoms in close vicinity to the defect is taken into account (blue line on Figure 4c): the intensity of peaks A and B_2 is somewhat decreased, while that of peak B_1 is increased as compared to the corresponding peaks in STO. While not vanishing completely, peak C is essentially suppressed. Looking at the single components of the total spectrum, calculated for each of the excited oxygen ions (denoted as O* in Figure 4c) in the close vicinity to the defect (atoms O_1, O_2, and O_3 on Figure 4a), one can clearly see that the changes in the spectrum are closely related with the number of Sr atoms around O and the corresponding Sr–O distances. We associate the suppression of peaks A and C with the presence of an additional Sr-ion (Sr''_{Ti}), which is at a rather short distance from the corresponding O (the $Sr''_{Ti} - O_1$ distance is ≈2.23 Å as compared to 2.75 Å in pristine STO). This conclusion is supported by our similar calculations for several Sr-rich phases (to be presented elsewhere), where additional Sr is always at short distance from the excited O atom. In contrast, the peak A in the spectrum of O_3 is practically unaffected by the presence of Sr''_{Ti}, because the corresponding $Sr''_{Ti} - O_1$ distance is significantly larger (≈2.74 Å) (the presence of V_O^{**} allows for the strong shift of the Sr''_{Ti} away from its initial position in the course of structural relaxation). As follows from our results, the change of the Ti–O bond length around the defect is rather small in contrast to Sr–O one (not more than 0.1 Å), and influences the O K-edge to a lesser extent.

However, when the contribution from the remaining O atoms in the supercell is taken into account together with the contributions from O_1, O_2, and O_3, the changes in the spectrum are less pronounced (red line in Figure 4c). This is obvious, since the spectra of the O atoms, situated further away from the defect, are less affected. This allows us to conclude that the concentration of such antisite defects in the sample should be rather high to cause the experimentally observed changes in the O K-edge spectrum.

4. Reversible Modifications under Applied Bias

Due to the low kinetic energy of the photoelectrons excited by soft X-rays and the correspondingly very short inelastic mean free path, the information depth of the photoemission Sr 3d

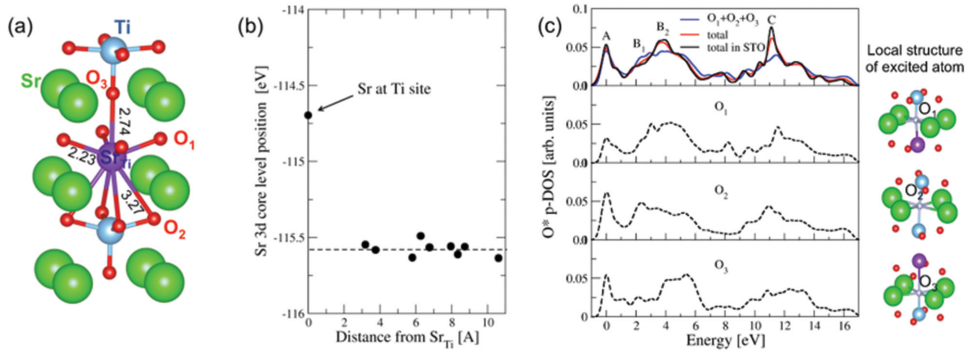

Figure 4. a) Structural model of the $SrTiO_3$ with Sr substituting a Ti ion accompanied by an oxygen vacancy ($Sr_{Ti}''-V_O^{**}$ antisite defect). b) Calculated Sr 3d core level position as a function of the distance from the antisite defect. The core level of Sr at Ti site is shifted by ≈0.8 eV to lower binding energy with respect to the more distant Sr. c) Total contribution to the densities of unoccupied *p*-states from all excited O* atoms (O K-edge spectra) in STO with (red line) and without (black line) $Sr_{Ti}''-V_O^{**}$ defect. The contribution from the 1st, 2nd, and 3rd nearest-neighbor O around the defect (atoms O_1, O_2, and O_3), weighted according to their number, is also shown (blue line). Black dashed lines represent the single contributions from each of the O_1, O_2, and O_3 excited atoms separately.

spectra obtained via PEEM is restricted to the surface layers and a few Å of subsurface region. However, the TEM cross-sectional analysis indicates that the deeper regions of the film are also of interest. In order to probe deeper into the MIM structures, we utilize hard X-ray photoelectron spectroscopy (HAXPES), which is a powerful technique to study buried interfaces due to the increasing inelastic mean free path of photoelectrons with higher kinetic energies.[34] Due to the large inelastic mean free path (IMFP), the electrode removal is no longer necessary and we can probe the chemical state of the devices through the top electrode.

In order to investigate MIM structures buried underneath the top electrode, we utilized a thin (50 Å) Rh layer as the top electrode. Rh is chemically similar to Au, but is a much weaker absorber for photoelectrons due to the smaller atomic weight. At the photoelectron kinetic energies between 4.9 and 5.4 keV used for this study, the inelastic mean free path λ can be estimated to be approximately $\lambda_{Rh} = 50$ Å in Rh and $\lambda_{STO} = 80$ Å in $SrTiO_3$, as calculated by the TPP2M code.[35] The information depth where 95% of the spectral intensity derives from would then be 16 nm for the STO film ($\lambda_{Rh} + 2\,\lambda_{STO}$) for normal emission. However, the spectral weight decreases exponentially away from the surface. The take-off angle (TOA) has been adjusted in order to increase sensitivity to the interface layer (TOA = 45°) or the bulk of the film (TOA = 2°).

Since HAXPES is an area-averaging technique, we examined large arrays for each resistive state, each consisting of over 4000 single devices with a size of 10 µm × 10 µm each. Within each array, all devices were switched with an identical voltage treatment. As can be seen from the statistical analysis in **Figure 5**a, reliable switching with reasonable pad-to-pad reproducibility and an R_{OFF}/R_{ON} ratio of roughly two orders of magnitude was achieved.

In order to study the reversible modifications of the chemical state under applied bias, we compare the spectroscopic signature of electrode arrays in the virgin state, ON state and OFF state. As depicted in Figure 5b, the Ti 2p XPS signal shows a single emission doublet, as is expected for STO, but with a substantial broadening compared to a single crystalline reference sample. This is likely an effect of slightly different chemical environments of Ti-ions in the probed volume.[36] However, no significant deviations can be observed in the Ti 2p spectrum between the different arrays. The same observation holds for the O 1s line (not shown).

In contrast, considerably differences are detected for the Sr 3d spectra (**Figure 6**). Using the same peak-fitting routine as

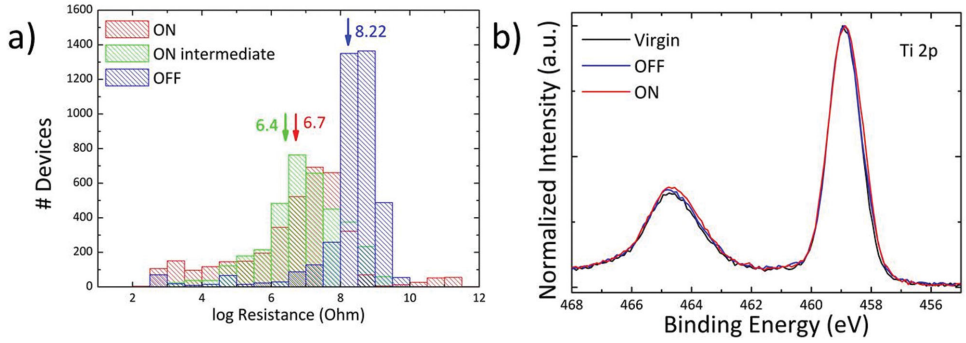

Figure 5. a) Resistance histogram of the switched arrays studied with HAXPES. The switching was performed with a Set voltage of +6 V and a Reset voltage of −7 V. "ON intermediate" denotes the resistance state of the OFF electrodes before the Reset process. b) Ti 2p XPS signal for virgin, ON, and OFF state reveals no significant difference.

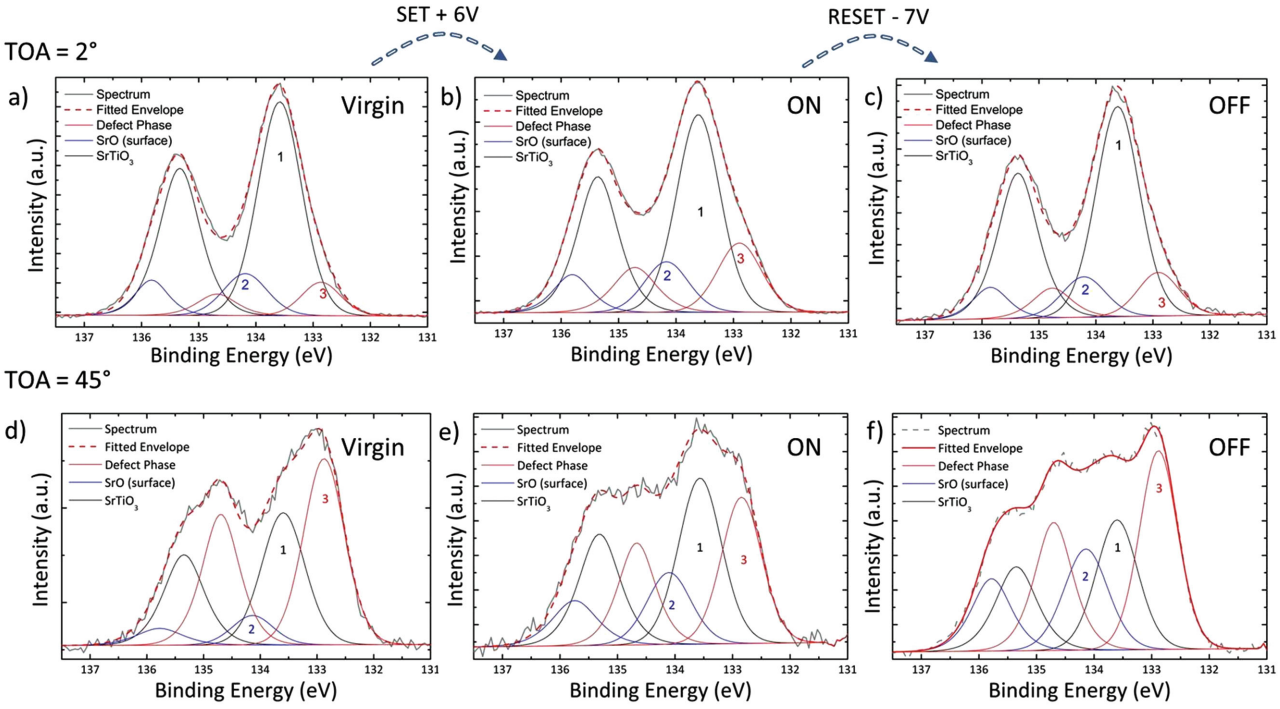

Figure 6. Sr 3d spectra and their constituent components as determined by peak-fitting analysis for the electrode arrays in virgin, ON and OFF state with a–c) 2° TOA and d–f) 45° TOA. Lineshape parameters (energy position, LG-mix, FWHM, area ratio, spin-orbit splitting, and relative energy separation between components) were fixed to values determined from NbSTO and FeSTO references for components 1 and 2, while the parameters for component 3 were varied within narrow regions.

described for the PEEM Sr XPS, we find three doublet components in each spectrum, consistent with the PEEM analysis. The low binding energy component "3" is located 0.7 eV below the emission lines from the STO lattice and shows a systematic variation between the different resistance states.

The intensity of this additional component is also clearly increased for the interface sensitive measurements, suggesting that component "3" is mainly concentrated at the film surface. We note that the discrepancy to the energy separation in the PEEM spectra (0.8 eV) is most likely a result of the reduced energy resolution of the PEEM, making the spectral deconvolution less precise.

Careful analysis reveals that while all three components are present in all spectra, the low-binding energy component 3 has greater spectral weight for the ON state measured under 2°, as compared to both OFF and virgin states. While the changes in the bulk-sensitive 2° TOA spectra are relatively small, the increased sensitivity to the electrode/oxide interface under 45° TOA reveals that the changes in the Sr chemistry are likely localized close at the interface. While the spectra for virgin and OFF state are dominated by component 3, the ON state spectrum shows a comparative decrease of component 3.

The comparison of bulk- and interface-sensitive spectra reveals that the low binding energy component 3 is initially localized at the electrode/metal interface in the virgin state, and pushed away from the interface and into the bulk upon application of a positive bias to the metal electrode. Reversing the bias depletes the bulk and again accumulates component 3 at the interface. This indicates a reversible change in the Sr chemical environment upon bipolar voltage treatment.

With regard to the spectral differences between the virgin and OFF spectra under 45°, we point out that the main difference is the amount of SrO (component 2) present at the interface. This is likely a result of thermal stress, which favors SrO segregation to the surface of STO and is not reversible.[22,37]

5. Discussion

To sum up our main experimental findings, we have established that Sr segregates to the surface during the forming process, during which a low binding energy component at the Sr 3d emission line is created. We attribute this component to Sr antisite defects with an associated oxygen vacancy $Sr''_{Ti} - V_O^{**}$, based on the comparison of ab initio calculations with the Sr 3d binding energy and the O K-edge XAS. TEM cross-sections show an inverted, truncated cone that forms underneath the surface segregation, with the wider base at the top electrode (anode). The Sr 3d core level shows a clear intensity variation of the low binding energy component ("3") for different resistive states when investigated with HAXPES.

In a first step, we would like to mention that the antisite defect can also be created during thin film deposition already. Indeed, the sample analyzed with HAXPES shows the defect component already in the virgin state, whereas the PEEM sample shows the same component only after electroforming.

The two types of samples were deposited in different PLD chambers, with a different parameter set and therefore a different point defect configuration and non-stoichiometry. We stress that the observation of Sr movement in both types of samples strengthens our presented case of the occurrence of Sr segregation during the forming processes in FeSTO.

Before we are going to relate our results to one another and to findings known from the literature, we need to discuss briefly the conditions under which the forming and resistive switching has been conducted in our present study. The forming process is performed with positive bias at the top electrode and a current compliance of 10 mA, which is reached at a bias of 4 V. It should be kept in mind that, despite of the large top electrode, forming and resistive switching is confined to one (or few) thin filaments.[18,27,38] The confinement of the forming current leads to an extremely high local dissipation of power and correspondingly high temperatures.[17] In a previous study of FeSTO films on NbSTO substrates using similar forming conditions, a single discharge channel and a recrystallization of the FeSTO film were clearly observed, presumably after a melting process.[19,26]

The high temperature leads to the irreversible segregation of SrO and the formation of $Sr''_{Ti}-V_O^{**}$ antisite defect associates on the film surface, which produces Sr''_{Ti} by removing lattice Sr from the film. The amounts of $Sr''_{Ti}-V_O^{**}$ and SrO that is observed via XPS and HAXPES make up a significant percentage of the Sr on the sample surface. The Sr vacancies V''_{Sr} act either as acceptors in intrinsic STO, or can enable a transformation from electronic-compensation to V''_{Sr} compensation in donor-doped STO.[14,21] Considering that the bottom electrode is a donor-doped STO single crystal, a filament enriched with V''_{Sr} could enable the diffusion of Sr from the substrate to the film, given a sufficiently high mobility on the cation sublattice due to the high temperature. Furthermore, the presence of oxygen vacancies or extended defects, such as grain boundaries or dislocations, can significantly facilitate the transport of Sr.[39,40] The reaction mechanism for oxidation of NbSTO is

$$\begin{aligned} &Sr^{2+}Ti_{1-x}Nb_xO_3+\frac{y}{2}O_2 \\ &\leftrightarrow Sr^{2+}_{1-y}+Ti_{1-x}Nb_xO_3+y*V''_{Sr}+y*SrO_{surface} \end{aligned} \quad (1)$$

Considering that the NbSTO is covered by the FeSTO film and the surface segregation is located at the surface of Fe:STO, the most likely source for oxygen in this reaction is the FeSTO thin film

$$\begin{aligned} &Sr^{2+}Ti_{1-x}Nb_xO_3+y*O^x_{O,film} \\ &\leftrightarrow Sr^{2+}_{1-y}+Ti_{1-x}Nb_xO_3+y*V''_{Sr}+y*SrO_{surface} \end{aligned} \quad (2)$$

The local temperature increases within the filaments can provide sufficient mobility of Sr ions in the lattice, while the transition from electronic compensation toward vacancy compensation in the NbSTO substrate provides a driving force for the segregation of Sr on the film surface. The substrate is therefore a possible source for sustaining an enrichment of Sr on the thin film surface. This is scenario is further supported by the contrast differences in the NbSTO substrate observed by TEM (Figure 3).

The forming procedure creates both V''_{Sr} and $Sr''_{Ti}-V_O^{**}$ on the film surface. A recent study of the formation enthalpies for point-defects in STO found that the Sr antisite defect is the most stable defect for Sr-rich STO.[41] It therefore seems likely that the creation of $Sr''_{Ti}-V_O^{**}$ defect complexes is a product of Sr-excess in the film, either from Sr-excess after growth (Figure S1, Supporting Information) or diffusion of Sr-ions from the NbSTO substrate to the surface.

It is also possible to regard the antisite defect as a reaction intermediate for the formation of SrO on the surface. The $Sr''_{Ti}-V_O^{**}$ antisite defect has been discussed as a precursor to Ruddlesden–Popper (RP) phases in STO, which can be regarded as an ordered structure of such defects forming a crystallographic shear plane in the oxide lattice.[23] If we assume the antisite defect as an early stage of the SrO planes in RP-phases, then it is plausible to obtain antisite defects as a way of creating SrO surface phases while retaining the perovskite structure

$$2SrO \leftrightarrow Sr^x_{Sr}Sr''_{Ti}(2O^x_OV_O^{**}) \quad (3)$$

The TEM studies show that a "filament" in the shape of an inverted, truncated cone forms underneath the surface segregations. This area is enriched in point defects, which are very likely V''_{Sr} created by the mechanism discussed above. Concerning the electrical properties of this filament, we do not present direct proof of an increased electronic conductivity in this work. However, we can infer from the surface segregation that the temperature during forming must be locally very high, which is only possible through Joule heating in a filament of locally increased electronic conductivity. This is indirect evidence that these filaments provide increased electronic conductivity, which is in apparent contradiction with the presence of acceptor-type point defects, V''_{Sr}.

We argue, however, that the mobility of oxygen is much higher than that of Sr. During forming, anodic bias is applied to the top electrode, leading to a removal of oxygen from the oxide surface. A SEM image taken after forming and switching confirms that the electrode is perforated at several places (not shown here), making oxygen removal into the atmosphere very likely. If a sufficiently large amount of oxygen is removed into the atmosphere or into the SrO surface phases according to Equation (2), the donor character of the V_O^{**} can overcompensate the acceptor character of the V''_{Sr} in the filament. In other words, if there are more V_O^{**} than V''_{Sr} in the filament, it will shows increased (n-type) conductivity.

In addition, we observe a depletion of $Sr''_{Ti}-V_O^{**}$ defect complexes under anodic bias (ON state) at the top interface via HAXPES, and an agglomeration at the top interface under cathodic bias (OFF state). Since the switching polarity is in agreement with both a migration of oxygen vacancies away from the top interface and a migration of strontium vacancies toward the top interface under anodic bias, we can not distinguish which ionic species moves under applied bias during switching. Since V_O^{**} are much more mobile in the lattice than V''_{Sr} we would expect that our observation reflects the movement of V_O^{**} and, as a consequence, the formation of highly n-conducting filaments in accordance with the established understanding of filamentary VCM-type resistive switching.

The active role of the NbSTO substrate in the forming step implies that the bottom interface might play a role in the bipolar

switching of the device. In addition, the eightwise polarity of the switching (positive bias at top electrode –> ON, negative bias –> OFF) is in disagreement with an oxidation/reduction of the top interface, therefore the redox-process determining device resistance may very well take place at the bottom interface. However, since neither of the utilized spectroscopic methods is capable of supplying information about the bottom interface, we refrain from suggesting a possible switching mechanism at this point. More detailed information about the electronic state of the defect-rich filament is necessary, along with modeling of the transport properties of the bottom interface, before any model can be proposed. This is beyond the scope of this work, where we concentrate on describing our experimental findings of the cation-defect based filaments.

6. Conclusion

By combining an area-averaging and a spatially resolving X-ray photoemission technique with high resolution electron microscopy, we have investigated the Sr movement during the forming and switching process in noble metal (Au and Rh)/FeSTO/NbSTO MIM structures. We find that Sr segregates at the noble metal top electrode interface under the high local temperatures during the forming process, leading to precipitates in the shape of small spots. Presumably, the Sr stems from a Sr-excess in the film and/or from the NbSTO substrate. The spots consist of both SrO and Sr''_{Ti} antisite defects. The latter may form $Sr''_{Ti} - V_O^{**}$ defect associates, as we establish with XPS and ab inito calculations. Whereas the SrO formation is obviously an irreversible process which occurs during forming and repeated switching, the formation of $Sr''_{Ti} - V_O^{**}$ defect associates can be reversibly modified by the applied bias during resistive switching. Despite the experimental observation of acceptor-type point defects (Sr''_{Ti} and V''_{Sr}), we conclude from the increased conductivity after forming that electronically compensated oxygen vacancies are present in the defective regions, in sufficient quantity to induce n-type conductivity. The study reveals once more the complexity of the nanoionic redox-based resistive switching phenomena.

7. Experimental Section

Device Preparation: Epitaxial Fe-doped $SrTiO_3$ thin films with Fe-contents of 2% and 5% site-fraction (for PEEM and HAXPES, respectively) with a thickness of 20 nm were grown on conducting 0.5 wt% Nb-doped $SrTiO_3$ substrates (NbSTO), commercially available from Crystec, Germany) by pulsed laser deposition (PLD). The deposition parameters for the films studied by PEEM/HAXPES were set to a laser fluence of 0.7/0.8 J cm^{-2}, a substrate temperature of 800/700 °C, an oxygen partial pressure of 0.1/0.25 mbar and a repetition rate of 5 Hz. For the PEEM experiments, a 25 nm Au layer was sputter deposited and structured into 10 μm × 10 μm electrode pads by optical lithography. For the HAXPES experiments, a 5 nm thin Rh film was deposited by e-beam evaporation and fabricated into electrode arrays of 500 μm × 1000 μm, consisting of 45 × 90 devices. The dimensions of the individual devices is 10 μm × 10 μm, with a separation of 1–2 μm. Using an automated switching setup, two arrays were set into the ON and the OFF state while another array served as a virgin-state reference. All electrical measurements (PEEM and HAXPES samples) are referenced to a grounded bottom electrode, with bias applied to the top.

HAXPES: To set the samples into the ON state, a voltage pulse of +6 V was applied for 3 s or until the current compliance of 2 mA was reached, and a subsequent readout of 100 mV used to determine the resistance. Reset was achieved by a similar voltage pulse with −7 V for 3 s or until the current compliance (1 mA) was reached and subsequent readout. Prior to the RESET operation, each pad was set into the ON state with the same SET procedure described above. This "ON intermediate" state shows a comparable resistance distribution to the ON array, demonstrating that both ON and OFF array are very similar with regard to switching properties and can be used to directly compare the two states. The HAXPES experiments had been performed at beamline P09[42] of the PETRA III storage ring at HASYLAB (DESY, Hamburg) at a photon energy of $E_{ph} = 5500$ eV. A Si 311 monochromator and an analyzer pass-energy of 40 eV were used, resulting in an overall energy resolution of 350 meV as determined by the width of the Au Fermi edge. The take-off angle (measured toward the surface normal) was varied from 2° (normal emission) to 45° in order to reduce the probing depth a factor of 0.7. The photon beam was focused to ≈200 × 500 μm under normal incidence, therefore the HAXPES experiments average over all electrode pads in the arrays under grazing incidence and 45° angle-of-incidence.

PEEM: All PEEM experiments had been performed at the NanoESCA beamline at Elettra synchrotron laboratory (Trieste, Italy) using the endstation described elsewhere.[43] Prior to the PEEM analysis the Au top electrodes were removed ex situ by wiping with a cotton swab and the sample is loaded into the UHV system within a few minutes after delamination. The complete removal of the Au top electrode is checked by recording of the Au 4f XPS intensity on the former pad area peak and for all presented pads the absence of any gold signal has been verified. The spatial resolution was about 100 nm in absorption mode. All images were divided by an averaged image from the pre-edge region to remove any work-function contrast that might be present in the images.

TEM: Cross-sectional lamellae with [001] zone-axis were prepared by FIB using a FEI Helios NanoLab 400S (FEI Company, Hillsboro, OR, USA). A Pt layer was deposited on top of the delaminated FeSTO samples to protect the oxide from ions radiation damage. The lamellae were further thinned and cleaned by a Fischione Nanomill 1040 system (E.A. Fischione Instruments, Inc., Export, PA, USA). The TEM imaging was performed on an FEI Titan 80–300 microscope equipped with an image CS corrector, capable of a spatial resolution below 1 nm.

Calculations: Electronic structure and structural optimizations were performed using the GGA+U approximation with U_{eff} = 4 eV and PAW pseudopotentials, as implemented in the VASP code.[44] The 4 × 4 × 4 k-points mesh was used for the integration over the Brillouin zone and the kinetic energy cut-off of 520 eV. The core level positions were calculated in the initial state approximation as the eigenvalues of the corresponding Kohn–Sham states. As a first step, we have considered single neutral vacancies of O, Sr, and Ti. However, the calculated shift for the Sr 3d core level with respect to its position in STO turned out to be either into the wrong direction or significantly smaller than the experimentally observed one.

Acknowledgements

This work was mainly supported by the Deutsche Forschungsgemeinschaft (DFG) within the SFB 917. C.L acknowledges for financial support from EC FP7 MATERA project "Functional materials for resistive switching memories" (FMRSM) and the NWR Ziel 2 program. The HAXPES instrument at beamline P09 is jointly operated by the University of Würzburg (R. Claessen), the University of Mainz (C. Felser), and DESY. Funding by the Federal Ministry of Education and Research (BMBF) under Contract Nos. 05KS7UM1, 05K10UMA, 05KS7WW3, and 05K10WW1 is

gratefully acknowledged. The authors would furthermore like to thank the beamline staff Dr. Andrei Gloskovskii for technical support.

Received: March 3, 2015
Revised: April 22, 2015
Published online: May 18, 2015

[1] A. Beck, J. G. , Bednorz, C. Gerber, C. Rossel, D. Widmer, *Appl. Phys. Lett.* **2000**, *77*, 139.
[2] R. Waser, M. Aono, *Nat. Mater.* **2007**, *6*, 833.
[3] A. Sawa, *Mater. Today* **2008**, *11*, 28.
[4] R. Waser, R. Dittmann, G. Staikov, K. Szot, *Adv. Mater.* **2009**, *21*, 2632.
[5] J. S. Lee, S. B. Lee, B. Kahng, T. W. Noh, *Appl. Phys. Lett.* **2013**, *102*, 253503.
[6] S. Kim, S. Choi, W. Lu, *ACS Nano* **2014**, *8*, 2369.
[7] D. B. Strukov, G. S. Snider, D. R. Stewart, R. S. Williams, *Nature* **2008**, *453*, 80.
[8] A. Mueller, K. Haerdtl, *Appl. Phys. A* **1989**, *49*, 75.
[9] R. Waser, *J. Am. Ceram. Soc. U.S.A.* **1991**, *74*, 1934.
[10] R. Merkle, J. Maier, *Angew. Chem. Int. Ed.* **2008**, *47*, 3874.
[11] M. Schie, A. Marchewka, T. Mueller, R. A. De Souza, R. Waser, *J. Phys.: Condens. Matter* **2012**, *24*, 485002.
[12] R. Meyer, R. Waser, J. Helmbold, G. Borchardt, *Phys. Rev. Lett.* **2003**, *90*, 105901.
[13] R. Wernicke, *Phys. Status Solidi A* **1978**, *47*, 139.
[14] D. M. Smyth, *Curr. Opin. Solid State Mater. Sci.* **1996**, *1*, 692.
[15] B. P. Andreasson, M. Janousch, U. Staub, T. Todorova, B. Delley, G. I. Meijer, E. Pomjakushina, *Phys. Rev. B* **2009**, *80*, 212103.
[16] B. P. Andreasson, M. Janousch, U. Staub, I. G. Meijer, *Appl. Phys. Lett.* **2009**, *94*, 13513.
[17] S. Menzel, M. Waters, A. Marchewka, A. Böttger, R. Dittmann, R. Waser, *Adv. Funct. Mater.* **2011**, *21*, 4487.
[18] C. Lenser, M. Patt, S. Menzel, C. Köhl, A Wiemann, C. Schneider, C. M. Waser, R. Dittmann, *Adv. Funct. Mater.* **2014**, *24*, 4466.
[19] R. Dittmann, R. Muenstermann, I. Krug, D. Park, T. Menke, J. Mayer, A. Besmehn, F. Kronast, C. M. Schneider, R. Waser, *Proc. IEEE* **2012**, *100*, 1979.
[20] Y. S. Kim, J. Kim, M. J. Yoon, C. H. Sohn, S. B. Lee, D. Lee, B. C. Jeon, H. K. Yoo, T. W. Noh, A. Bostwick, E. Rotenberg, J. Yu, S. D. Bu, B. S. Mun, *Appl. Phys. Lett.* **2014**, *104*, 13501.
[21] R. Meyer, R. Waser, J. Helmbold, G. Borchardt, *J. Electroceram.* **2002**, *9*, 101.
[22] K. Szot, W. Speier, U. Breuer, R. Meyer, J. Szade, R. Waser, *Surf. Sci.* **2000**, *460*, 112.
[23] D. Fuchs, M. Adam, P. Schweiss, S. Gerhold, S. Schuppler, R. Schneider, B. Obst, *J. Appl. Phys.* **2000**, *88*, 1844.
[24] B. Rahmati, J. Fleig, W. Sigle, E. Bischoff, J. Maier, M. Rühle, *Surf. Sci.* **2005**, *595*, 115.
[25] K. Szot, W. Speier, *Phys. Rev. B: Condens. Matter* **1999**, *60*, 5909.
[26] R. Muenstermann, T. Menke, R. Dittmann, R. Waser, *Adv. Mater.* **2010**, *22*, 4819.
[27] C. Lenser, A. Kuzmin, J. Purans, A. Kalinko, R. Waser, R. Dittmann, *J. Appl. Phys.* **2012**, *111*, 76101.
[28] M. Abbate, F. M. F. de Groot, J. C. Fuggle, A. Fujimori, Y. Tokura, Y. Fujishima, O. Strebel, M. Domke, G. Kaindl, J. van Elp, B. T. Thole, G. A. Sawatzky, M. Sacchi, N. Tsuda, *Phys. Rev. B* **1991**, *44*, 5419.
[29] E. Breckenfeld, R. Wilson, J. Karthik, A. R. Damodaran, D. G. Cahill, L. W. Martin, *Chem. Mater.* **2012**, *24*, 331.
[30] F. M. F. de Groot, J. Faber, J. J. M. Michiels, M. T. Czyżyk, M. Abbate, J. C. Fuggle, *Phys. Rev. B* **1993**, *48*, 2074.
[31] D. Keeble, S. Wicklein, R. Dittmann, L. Ravelli, R. A. Mackie, W. Egger, *Phys. Rev. Lett.* **2010**, *105*, 4.
[32] T. Fujikawa, *J. Phys. Soc. Jpn.* **1983**, *52*, 4001.
[33] H. P. Hjalmarson, H. Büttner, J. D. Dow, *Phys. Rev. B* **1981**, *24*, 6010.
[34] C. Fadley, *Nucl. Instrum. Methods Phys. Res., Sect. A* **2005**, *547*, 24.
[35] S. Tanuma, C. J. Powell, D. R. Penn, *Surf. Interface Anal.* **1994**, *21*, 165.
[36] S. Stille, C. Lenser, R. Dittmann, A. Koehl, I. Krug, R. Muenstermann, J. Perlich, C. M. Schneider, U. Klemradt, R. Waser, *Appl. Phys. Lett.* **2012**, *100*, 223503.
[37] Y. Chen, W. Jung, Z. Cai, J. J. Kim, H. L. Tuller, B. Yildiz, *Energy Environ. Sci.* **2012**, *5*, 7979.
[38] A. Koehl, H. Wasmund, A. Herpers, P. Guttmann, S. Werner, K. Henzler, H. Du, J. Mayer, R. Waser, R. Dittmann, *APL Mater.* **2013**, *1*,042102.
[39] A. Walsh, C. R. A. Catlow, A. G. H. Smith, A. A. Sokol, S. M. Woodley, *Phys. Rev. B* **2011**, *83*, 220301.
[40] J. W. C. de Vries, R. M. Waser, *Proc. 7th IEEE Int. Symp. Appl. Ferroelectr.* IEEE, New York **1991**, pp 557–561.
[41] B. Liu, V. R. Cooper, H. Xu, H. Xiao, Y. Zhang, W. J. Weber, *Phys. Chem. Chem. Phys.* **2014**, *16*, 15590.
[42] A. Gloskovskii, G. Stryganyuk, G. H. Fecher, C. Felser, S. Thiess, H. Schulz-Ritter, W. Drube, G. Berner, M. Sing, R. Claessen, M. Yamamoto, *J. Electron Spectrosc. Relat. Phenom.* **2012**, *185*, 47.
[43] C. Wiemann, M. Patt, I. P. Krug, N. B. Weber, M. Escher, M. Merkel, C. M. Schneider, *e-J. Surf. Sci. Nanotechnol.* **2011**, *9*, 395.
[44] G. Kresse, J. Furthmüller, *Phys. Rev. B* **1996**, *54*, 11169.